

Clock offset recovery with sublinear complexity enables synchronization on low-level hardware for quantum key distribution

Jan Krause ,* Nino Walenta , Jonas Hilt, and Ronald Freund 

Fraunhofer Institute for Telecommunications, Heinrich-Hertz-Institut, HHI, 10587 Berlin, Germany

(Dated: Friday 5th April, 2024)

We introduce iQSync, a clock offset recovery method designed for implementation on low-level hardware, such as FPGAs or microcontrollers, for quantum key distribution (QKD). iQSync requires minimal memory, only a simple instruction set (e.g. no floating-point operations), and can be evaluated with sublinear time complexity, typically involving no more than a few thousand iterations of a simple loop. Furthermore, iQSync allows for a precise clock offset recovery within few seconds, even for large offsets, and is well suited for scenarios with high channel loss and low signal-to-noise ratio, irrespective of the prepare-and-measure QKD protocol used. We implemented the method on our QKD platform, demonstrating its performance and conformity with analytically derived success probabilities for channel attenuations exceeding 70 dB.

I. INTRODUCTION

Quantum key distribution (QKD) allows for the generation of symmetric cryptographic keys between two remote parties with information-theoretical protocol security [1, 2]. In contrast to conventional optical communication, QKD is based on the transmission and detection of single photons, which complicates the required precise clock synchronization between sender (Alice) and receiver (Bob). Bob typically only receives a small fraction of the symbols transmitted by Alice, usually in the range of 1/10 to 1/10⁷ [3]. Additionally, the quantum bit error rate (QBER) can reach up to approximately

11 % [4], substantially exceeding typical bit error rates of 10⁻⁹ or less encountered in classical fiber-optical communication systems [5]. These conditions prevent the usage of established synchronization methods from classical telecommunication and therefore necessitate the usage of different approaches.

Conceptually, the task of clock synchronization between Alice and Bob can be divided into *clock phase-locking*, i.e. ensuring that both clocks operate at the exact same frequency, and *clock-offset recovery*, needed for Bob to assign the correct qubit index to each detected photon. Ideally, a synchronization method also provides the ability to identify large clock offsets, reliable operation, high precision, fast completion within seconds even for high transmission losses, algorithmic simplicity, low resource usage, low cost of the required components, and no dependence on third-party infrastructure like GPS satellites.

Clock phase-locking can be realized through transmission of Alice's clock beat via a dedicated clock channel [6–14], by using (GPS-disciplined) atomic clocks [15–18], or by exploiting the timing characteristics of single-photon detections, which was demonstrated for entanglement-based systems [19–21], as well as for prepare-and-measure systems [22–29].

Clock offset recovery is mostly performed via single-photon detections in the quantum channel with approaches existing for entanglement-based systems [17–21, 30–32], and for prepare-and-measure systems [22–27, 33, 34]. While methods employing the classical channel exist [13, 14], they introduce additional routing constraints.

One of the simplest approaches for clock offset recovery via single-photon detections in the quantum channel employs a fast Fourier transform (FFT) [35] with time complexity (TC) in $\mathcal{O}(n \log_2 n)$, where n corresponds to the maximum recoverable offset. For typical offsets of up to multiple 100 ms and sub-nanosecond symbol durations [3], this imposes high demands on CPU and RAM. Furthermore, calculation of the FFT requires floating-point operations and substantial resources on platforms like FPGAs.

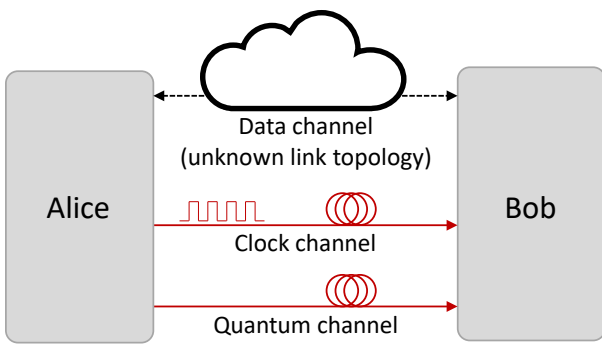


FIG. 1. A typical QKD setup. Qubits, e.g. encoded in coherent quantum states with low mean photon number $\mu \lesssim 1$, are transmitted from Alice to Bob using a *quantum channel*. Due to channel losses, Bob usually receives states with $\mu \ll 1$. A *bi-directional data channel* with high (e.g. a few hundred ms) unknown and undeterministic (but bounded) latencies is used for classical communication between Alice and Bob, and for QKD post-processing. An optional *clock channel* is often used to establish a common clock phase.

* jan.krause@hhi.fraunhofer.de

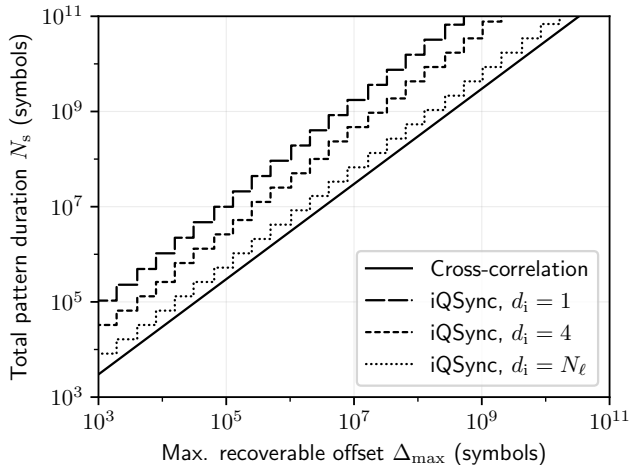


FIG. 2. Relation between the total synchronization pattern duration N_s and the max. recoverable offset Δ_{\max} for different degrees of interleaving d_i . Cross-correlation refers to approaches utilizing a single FFT, or the dual-step FFT approach as presented in [23].

An approach with reduced TC of $\mathcal{O}(n \log_2 \log_2 n)$ was presented in 2020 by Calderaro et al. [23]. It uses a random pattern that is constructed such that two FFTs on reduced datasets can be calculated. However, it still requires FFTs on large datasets and floating-point operations, hindering its usage on low-level hardware.

Another approach, proposed by Braithwaite, uses a dichotomic search algorithm to consecutively reconstruct the bits of the binary representation of the clock offset, starting from the least significant bit [36]. It only requires simple computational instructions, i.e. no floating-point operations, at the expense of a pattern duration that scales super-linearly with the maximum recoverable offset as $\mathcal{O}(n \log_2 n)$. Furthermore, it requires the exchange of multiple confirmation messages between Alice and Bob.

Here, we propose iQSync, a synchronization method, which is also based on a consecutive bit-wise recovery of the clock offset, but uses random interleaving of the patterns required for the recovery of each bit. This approach allows for keeping a linear scaling $\mathcal{O}(n)$ of the overall synchronization pattern length, while offset recovery at Bob is reduced to sublinear TC.

The free choice of the degree of interleaving d_i allows for optimization of resources in any given hardware as well as finetuning of the trade-off between failure probability and required pattern duration.

Furthermore, not more than one single message needs to be transmitted from Alice to Bob at the beginning of the synchronization. The synchronization pattern can be generated and evaluated without complex calculations, using only few additions and bit-shifts within a loop. Also, storage of pre-computed patterns is not necessary for our method. Therefore, our method is ideally suited for cost-efficient implementation on low-level hardware.

Pattern generation and the dichotomic search offset recovery algorithm for iQSync are described in Section II and the success probability is analytically derived in Section III. The TC of iQSync is analyzed in Section IV. An experimental validation of these results is presented in Section V. Finally, Section VI concludes this work.

II. METHODS

A typical QKD setup is depicted in Fig. 1. While the quantum channel requires a direct optical connection, our method allows for the classical data channel to be routed over a separate link with varying, unknown (but bounded) latencies up to hundreds of milliseconds. In the following we assume that clock phase-locking is provided and focus on clock offset recovery.

Our method iQSync works as follows:

1. Alice and Bob agree on the maximum level $\ell_{\max} \in \mathbb{N}$, which defines the maximum recoverable offset Δ_{\max} , cf. Eq. (1). They furthermore agree on the degree of interleaving d_i . These values can be fixed and preconfigured.
2. Alice sends a start signal to Bob via the data channel, providing Bob with a coarse marker of the transmission beginning. This is the only classical message needed for iQSync.
3. At the same time, Alice starts the transmission of the synchronization pattern over the quantum channel, described in Section II A.
4. Upon reception of the start signal, Bob starts to acquire single photon detections and to analyze these according to the algorithm described in Section II B.

Pattern generation and offset recovery are described in Sections II A and II B respectively.

An example Python implementation is given in the Supplemental Material [37].

A. Pattern generation (Alice)

The pattern transmitted by Alice can be generated during live operation with very few operations per symbol.

The synchronization pattern is divided into multiple *levels*. Each, except for level 0, is used to obtain one bit of the binary signed integer representation of the clock offset in symbol precision. Level 0 consists of the symbol 0 only and is needed for systems which use more than one timebin to encode a symbol or qubit, e.g. timebin-phase QKD systems [38, 39], to obtain proper symbol alignment.

Although different encodings can be used, symbols should not be encoded via the absence of optical pulses,

TABLE I. Example symbol pattern for iQSync, using a maximum level $\ell_{\max} = 2$, and the degree of interleaving $d_i = 1$ (no interleaving). Each level consists of $N_{s,\ell} = 2^{\ell_{\max}+1}$ symbols and is used to reconstruct one bit of the binary integer representation of the clock offset. Level 0 is only needed in case a symbol is encoded in more than one timebin, as is the case for our implementation. An algorithmic description of the pattern generation is given in Algorithm 1.

Symbol index k	0	1	2	3	4	5	6	7	8	9	10	11	12	13	14	15	16	17	18	19	20	21	22	23
Level ℓ	0	0	0	0	0	0	0	0	1	1	1	1	1	1	1	1	2	2	2	2	2	2	2	2
Symbol s	0	0	0	0	0	0	0	0	0	1	0	1	0	1	0	1	0	0	1	1	0	0	1	1

TABLE II. Example symbol pattern for iQSync, using a maximum level $\ell_{\max} = 3$, and the degree of interleaving $d_i = 2$. Each group (separated by the vertical line) is constructed from $d_i = 2$ interleaved levels by randomly choosing the level from which to take the symbol value for each symbol. An algorithmic description of the pattern generation is given in Algorithm 1. Intermediate steps for offset recovery are given in the lower half and described in Sec. II B.

Symbol index k	0	1	2	3	4	5	6	7	8	9	10	11	12	13	14	15	16	17	18	19	20	21	22	23	24	25	26	27	28	29	30	31
Group index g	0															1																
Symbol for $\ell = 0$	0	0	0	0	0	0	0	0	0	0	0	0	0	0	0																	
Symbol for $\ell = 1$	0	1	0	1	0	1	0	1	0	1	0	1	0	1	0																	
Symbol for $\ell = 2$																0	0	1	1	0	0	1	1	0	0	1	1	1				
Symbol for $\ell = 3$																0	0	0	0	1	1	1	0	0	0	0	1	1	1			
Randomly chosen ℓ	0	0	1	0	1	1	1	1	0	0	1	0	1	1	0	1	3	2	2	3	2	2	2	3	2	2	3	3	2			
Transmitted symbol s	0	0	0	0	0	1	0	1	0	0	0	0	0	0	1	0	0	0	1	0	1	0	0	0	1	0	1	1	1			
R1: Received, 3 sym. offset	0	0	0	0	0	1	0	1	0	0	0	0	0	0	0	1	0	1	0	0	1	0	0	0	1	1	0	0	1	0		
R2: Acceptance windows	0	0	0	0	1	0	1	0															0	1	0	0	0	1	1	0		
R3: Contrib. to C for $\ell = 1$	1	-1	1	-1	-1	-1	-1	-1																								
R4: Shifted by $\delta_s = 1$	0	0	0	0	1	0	1	0															0	1	0	0	0	1	1	0		
R5: Contrib. to C for $\ell = 2$																1																
R6: Shifted by $\delta_s = 1$	0	0	0	0	0	1	0	1	0															0	1	0	0	0	1	1	0	
R7: Contrib. to C for $\ell = 3$																-1																

e.g. via on-off keying, but via codings for which the channel attenuation does not introduce an asymmetry in the detected bit values, e.g. pulse-position modulation (PPM) or polarization coding.

Examples for patterns without and with interleaving are given in Table I and Table II, and general pattern generation, including level 0, is described in Algorithm 1. Variables are initialized in lines 1-4, where N_ℓ is the total amount of levels, interleaved in N_g groups of d_i levels. Each group has $N_{s,g}$ symbols, leading to the total amount of N_s symbols. A loop iterates over all symbols (line 5). Out of the levels of the current group, a random level ℓ is chosen (lines 6-9), and the ℓ 'th least significant bit of the current symbol index is chosen for the transmitted symbol.

Recoverable offsets Δ in units of the symbol duration are limited by

$$-\Delta_{\max} \leq \Delta < \Delta_{\max} - 1 \quad , \text{with} \quad (1)$$

$$\Delta_{\max} = 2^{\ell_{\max}-1}, \quad (2)$$

cf. Fig. 2. Hence, the total pattern duration scales as

$\mathcal{O}(n \log_2 n)|_{n=\Delta_{\max}}$ for $d_i = 1$ (no interleaving), and as $\mathcal{O}(n)|_{n=\Delta_{\max}}$ for $d_i = N_\ell$ (maximum interleaving). A version similar to [36] is obtained for $d_i = 1$.

When choosing d_i as a power of two, Algorithm 1 only requires bit-shifts and additions which enables straightforward implementation on low-level hardware, like microcontrollers or FPGAs.

The time required for the transmission of the synchronization pattern is given by

$$T = N_s t_s, \quad (3)$$

where t_s is the symbol duration.

B. Offset recovery (Bob)

To recover the clock offset, the detected pattern is evaluated at Bob in two steps.

First, Bob determines the shift necessary to align the detections to the timebins, e.g. by employing a histogram. This step defines the overall precision of the syn-

Algorithm 1 Pattern generation for iQSync. The pattern depends on the maximum level ℓ_{\max} , and the degree of interleaving d_i . Both values should be chosen such that the max. recoverable offset is sufficiently large, cf. eq. (1), and the detection statistics leads to a sufficiently high success probability, cf. Section III. An example pattern for $\ell_{\max} = 3$ and $d_i = 2$ is shown in Table II. LSB: Least significant bit; \ll, \gg : Bit shifts.

Input: ℓ_{\max}	▷ Max. level
Input: d_i	▷ Degree of interleaving
1: $N_\ell \leftarrow \ell_{\max} + 1$	▷ Number of levels
2: $N_g \leftarrow \lceil N_\ell / d_i \rceil$	▷ Number of groups
3: $N_{s,g} \leftarrow 2^{\ell_{\max}+1}$	▷ Number of symbols per group
4: $N_s \leftarrow N_{s,g} \times N_g$	▷ Total pattern duration (symbols)
5: for $k_s \leftarrow 0$ to $N_s - 1$ do	
6: $k_g \leftarrow k_s \gg N_\ell$	▷ Index of current group
7: $\ell^- \leftarrow k_g \times d_i$	▷ Min. level in group
8: $\ell^+ \leftarrow \min(\ell^- + d_i - 1, \ell_{\max})$	▷ Max. level in group
9: $\ell \leftarrow \text{randint} \in \{\ell^-, \dots, \ell^+\}$	▷ Chosen level
10: $s \leftarrow \text{LSB}((k_s \ll 1) \gg \ell)$	▷ Select symbol
11: transmit symbol s	

chronization in the sub-timebin regime. Subsequently, this shift is applied to all detections. Bob then converts all detection timestamps to timebin precision using remainder-free division by the timebin duration.

Secondly, the clock offset in timebin granularity is reconstructed using the dichotomic search Algorithm 2, which assumes binary PPM coding with the bit one encoded as a late pulse. The variable initialization in lines 1-2 is analog to Algorithm 1. The total reconstructed offset in timebin granularity is stored in δ . The offset in symbol precision is given by $\delta_s = \delta/2$.

The outer loop (line 7-29) iterates over all levels, with the currently analyzed level stored in ℓ . The counter variable C stores the difference of the correct and wrong symbols of the current level. At the end of the evaluation of each level the counter is used to update the offset δ , if $C < 0$ (lines 28-29).

The inner loop (line 10-27) is used to determine C by iterating over the detections belonging to the currently analyzed level. This is achieved using the acceptance window defined by k_s^- and k_s^+ in lines 3-4, which is applied to each group in lines 18-20. The remaining detections are ensured to belong to the assumed level, given that the actual offset $|\Delta_{\text{actual}}| < \Delta_{\max}$ symbols, cf. Eq. (1). The current symbol is shifted according to the already recovered offset (line 21), and the counter C is increased (decreased) in lines 26-29, in case the symbol corresponds to the expected/correct (unexpected/wrong) symbol.

Finally, lines 30-33 ensure that the reconstructed offset δ falls into the range $[-2\Delta_{\max}, 2\Delta_{\max} - 1]$, and is positive in case Bob's clock is running ahead.

Note that this algorithm only uses integer variables and requires no complex instructions like floating point

Algorithm 2 Offset recovery for iQSync. The algorithm assumes binary PPM coding. As input it takes the maximum level ℓ_{\max} , the degree of interleaving d_i , and the timebin indices for which detections were obtained. It returns the clock offset δ in timebin precision. If Bob's clock is running ahead, $\delta > 0$, cf. Section II B.

Input: ℓ_{\max}	▷ Max. level
Input: d_i	▷ Degree of interleaving
Input: \mathcal{D}	▷ Detection timebin indices
1: $N_\ell \leftarrow \ell_{\max} + 1$	▷ Number of levels
2: $N_{s,g} \leftarrow 2^{\ell_{\max}+1}$	▷ Number of symbols per group
3: $k_s^- \leftarrow 2^{\ell_{\max}-1}$	
4: $k_s^+ \leftarrow N_{s,g} - 2^{\ell_{\max}-1}$	
5: $\delta \leftarrow 0$	▷ Recovered offset
6: $k^- \leftarrow 0$	▷ Index of first detection of current group
7: for $\ell \leftarrow 0$ to ℓ_{\max} do	▷ Iterate over all levels
8: $C \leftarrow 0$	▷ Counter
9: $g_{\text{req}} \leftarrow \lfloor \ell / d_i \rfloor$	
10: for $k \leftarrow k^-$ to $ \mathcal{D} - 1$ do	
11: $k_s \leftarrow \mathcal{D}(k) /2$	▷ Current symbol index
12: $g \leftarrow k_s \gg N_\ell$	▷ Current group
13: if $g > g_{\text{req}}$ then	
14: $g_{\text{req,next}} \leftarrow \lfloor (\ell + 1) / d_i \rfloor$	
15: if $g_{\text{req,next}} > g_{\text{req}}$ then	
16: $k^- \leftarrow k$	
17: break	
18: $k_{s,g} \leftarrow$ the N_ℓ LSBs of k_s ▷ Symb. idx. i. group	
19: if $k_{s,g} < k_s^-$ or $k_{s,g} \geq k_s^+$ then	
20: continue	
21: $k_{s,\text{shifted}} \leftarrow [\mathcal{D}(k) + \delta] \gg 1$	
22: $s_{\text{expected}} \leftarrow \text{LSB}((k_{s,\text{shifted}} \ll 1) \gg \ell)$	
23: $s \leftarrow \text{LSB}(\mathcal{D}(k) + \delta)$	
24: if $s = s_{\text{expected}}$ then	
25: $C \leftarrow C + 1$	
26: else	
27: $C \leftarrow C - 1$	
28: if $C < 0$ then	
29: $\delta \leftarrow \delta + 2^\ell$	
30: if $\delta > 2^{\ell_{\max}}$ then	
31: $\delta \leftarrow \delta - 2^{\ell_{\max}+1}$	
32: $\delta \leftarrow -\delta$	
33: return δ	

operations, but only additions and bit-shifts, since all multiplications and divisions by base-2 powers can be replaced by bit-shifts. Thus, the algorithm is ideally suited for the implementation on FPGAs or microcontrollers.

A step-by-step example for offset recovery, using $\ell_{\max} = 3$ and $d_i = 2$, is given in Table II, where it is assumed that Bob's clock runs ahead by 3 symbols ($\Delta = 3t_s$), cf. step R1 in Table II. For simplicity, the example assumes that no signals are lost, and the recovery for $\ell = 0$ is omitted, i.e. proper symbol alignment is assumed. Application of the acceptance windows (lines 19-20 of Algorithm 2) removes the detections from the first and last quarter of each group (R2). Then, level 1 is evaluated (R3). Therefore, the counter C is increased

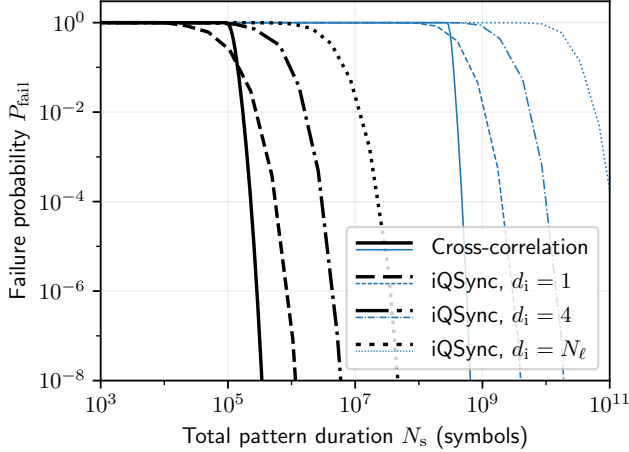


FIG. 3. Calculated synchronization failure probability P_{fail} for two experimental conditions, depending on the total pattern duration N_s . The thick black lines depict a scenario with high signal and low noise detection probability ($p_{\text{sig}} = 10^{-3}$, $p_{\text{noise}} = 10^{-7}$). The thin blue lines represent low signal and high noise detection probability ($p_{\text{sig}} = p_{\text{noise}} = 10^{-6}$). Cross-correlation refers to approaches utilizing a single FFT and the dual-step FFT approach as presented in [23].

(decreased) by 1 for each received symbol that matches (differs from) the expected symbol (lines 24-27 in Algorithm 2). Since $C = -4 < 0$ (sum over all values in R3), the recoverd offset δ is increased to $2^\ell = 2$ (symbol offset $\delta_s = \delta/2 = 1$), cf. lines 28-29 in Algorithm 2. For the evaluation of level 2 the received symbols are then shifted by δ_s (R4, line 23 in Algorithm 2), and C is again evaluated (R5). Since counter $C = 6 \geq 0$, the offset δ (δ_s) remains unchanged. The evaluation of level 3 (R6, R7) leads to $C = -2 < 0$, and the offset is uptated to $\delta = 10$ ($\delta_s = 5$). Finally, since $\delta > 2^{\ell_{\max}} = 8$, the offset is reduced by $2^{\ell_{\max}+1} = 16$, and its sign is inverted (lines 30-32 in Algorithm 2), leading to $\delta = 6$ ($\delta_s = 3$). Hence, the correct offset is identified.

III. SUCCESS PROBABILITY

The success probability of the described method depends on the single-photon detection statistics. To facilitate the straightforward identification of appropriate parameters ℓ_{\max} and d_i , an analytical expression for the success probability in terms of the signal (noise) detection probability per symbol p_{sig} (p_{noise}) is derived in the following. It is also the basis for the average-case TC analysis in Sec. IV.

The amount of symbols per group is given by

$$N_{s,g} = 2^{\ell_{\max}+1}. \quad (4)$$

The amount of signal detections, and hence the contribution to the counter C (cf. Algorithm 2) per level is

described by a Binomial distribution

$$C_{\text{sig}} \sim B \left(\frac{N_{s,g}}{2}, p_{\text{sig}} \frac{1}{d_i} \right), \quad (5)$$

where the factor of $1/2$ was added, because the first and last quarter of each group are removed by the acceptance window (cf. Section II B). The probability for a signal detection per symbol is denoted as p_{sig} and the factor $1/d_i$ describes the fact that only signals from the currently analyzed level contribute constructively, while all other interleaved levels lead to random detections. The influence of random detections onto the counter is given by

$$C_{\text{rand}} = N_{\text{rand},+} - N_{\text{rand},-}, \quad (6)$$

with

$$N_{\text{rand},\pm} \sim B \left(\frac{N_{s,g}}{2}, \frac{1}{2} p_{\text{rand}} \right), \quad (7)$$

where

$$p_{\text{rand}} = 1 - (1 - p_{\text{noise}})[1 - p_{\text{sig}}(1 - 1/d_i)] \quad (8)$$

$$\stackrel{p_{\text{noise}}, p_{\text{sig}} \ll 1}{\approx} p_{\text{noise}} + p_{\text{sig}}(1 - 1/d_i),$$

and p_{noise} denotes the probability for a noise detection per symbol. Finally, the counter follows the distribution

$$C \sim C_{\text{sig}} + C_{\text{rand}}. \quad (9)$$

Approximating the Binomial distributions by normal distributions via [40]

$$B(n, p) \approx \mathcal{N}(np, np(1-p)) = \mathcal{N}(\mu, \sigma^2) \quad (10)$$

yields

$$C \sim \mathcal{N}(\mu_{\text{sig}}, \sigma_{\text{sig}}^2) + \mathcal{N}(\mu_{\text{rand},\pm}, \sigma_{\text{rand},\pm}^2) - \mathcal{N}(\mu_{\text{rand},\pm}, \sigma_{\text{rand},\pm}^2) \quad (11)$$

$$= \mathcal{N}(\mu_{\text{tot}}, \sigma_{\text{tot}}^2), \quad (12)$$

where

$$\mu_{\text{tot}} = \frac{N_{s,g}}{2} \frac{p_{\text{sig}}}{d_i} = \mu_{\text{sig}}, \quad (13)$$

$$\sigma_{\text{tot}}^2 = \sigma_{\text{sig}}^2 + 2\sigma_{\text{rand},\pm}^2, \quad (14)$$

$$\sigma_{\text{sig}}^2 = \frac{N_{s,g}}{2} \frac{p_{\text{sig}}}{d_i} \left(1 - \frac{p_{\text{sig}}}{d_i} \right), \quad (15)$$

$$\sigma_{\text{rand},\pm}^2 = \frac{N_{s,g}}{2} \frac{p_{\text{rand}}}{2} \left(1 - \frac{p_{\text{rand}}}{2} \right). \quad (16)$$

The probability for successful analysis of one level is then found as

$$P_{\text{success},1} = P(C > 0) \approx \Phi \left(\frac{\mu_{\text{tot}}}{\sigma_{\text{tot}}} \right), \quad (17)$$

where Φ is the cumulative distribution function of the standard normal distribution. This leads to the probability

$$P_{\text{success}} = P_{\text{success},1}^{N_\ell} \quad (18)$$

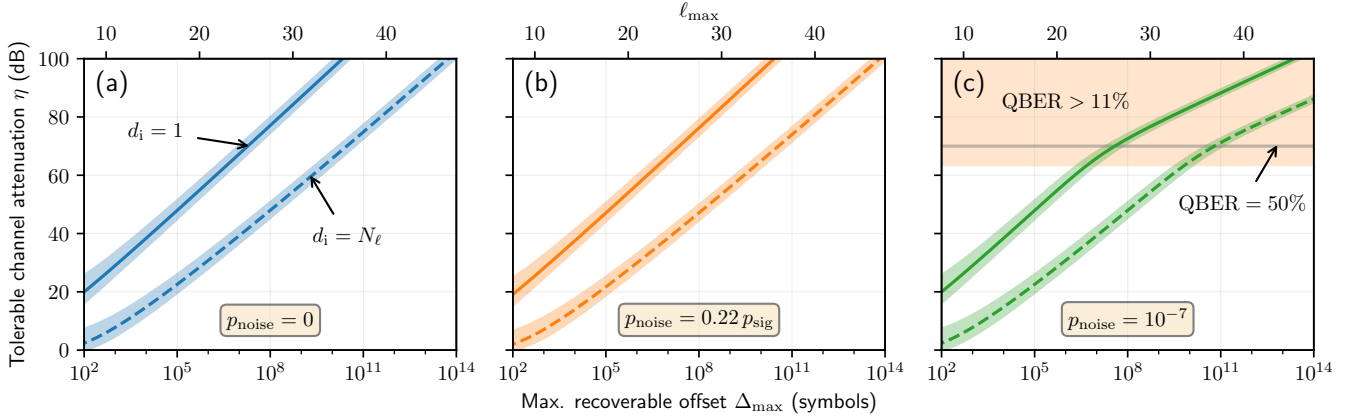


FIG. 4. Tolerable channel attenuation η for iQSync, depending on the maximum recoverable offset Δ_{\max} , the degree of interleaving d_i , and the probability for a noise detection per symbol p_{noise} . The solid (dashed) lines represent the settings with 50% success probability for no (maximal) interleaving, with the lower (upper) edge of the shaded areas marking the 90'th (10'th) success percentile. The case of no noise is depicted in (a). The most pessimistic scenario for QKD is shown in (b), where for each configuration a QBER of 11% is assumed. The case of $p_{\text{noise}} = 10^{-7}$ is shown in (c), representative for the detectors used during our experimental validation, cf. Section V. The position of the kink depends on p_{noise} and always sits at the point, where the channel transmission equals p_{noise} . The area with a QBER > 11% is shaded red.

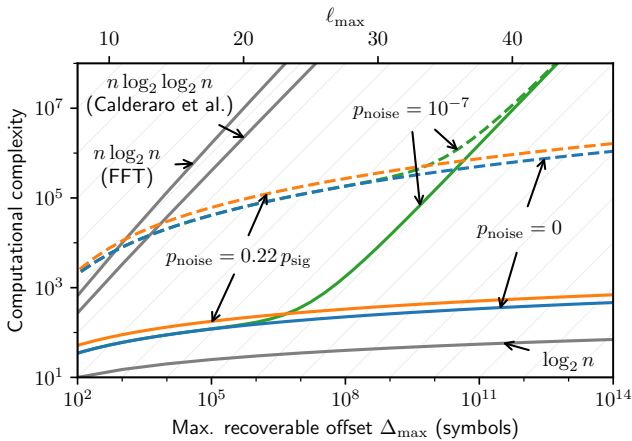


FIG. 5. TC of iQSync in terms of the number of iterations \bar{N}_{loop} over the inner loop of Algorithm 2 for different levels of noise, corresponding to the lines in Fig. 4. The solid (dashed) lines represent the settings with 50% success probability for no (maximal) interleaving. The three gray lines depict the TC of the FFT, the dual-step approach by Calderaro et al. [23], and the theoretical limit $\log_2 n$, given by the number of bits of the binary representation of the offset. The light gray lines depict linear TC as a reference.

for the whole synchronization to succeed.

For a given link, an increase of the degree of interleaving d_i leads to shorter synchronization patterns at the expense of higher failure probabilities, cf. Fig. 2, Fig. 3, and Fig. 7(b).

IV. TIME COMPLEXITY

The TC for pattern generation is given by the pattern duration, i.e. $\mathcal{O}(n \log_2 n)$ for $d_i = 1$, and $\mathcal{O}(n)$ for $d_i = N_\ell$, cf. Eq. (1) and Algorithm 1.

For the recovery algorithm the TC can be analyzed numerically, using the previously derived analytical expression for the success probability, leading to the channel attenuation

$$\eta = \eta(\ell_{\max}, d_i, p_{\text{noise}}, P_{\text{success}}). \quad (19)$$

Application of the constraint $P_{\text{success}} = 0.5$, used to establish a fair comparison, produces the lines shown for different configurations in Fig. 4. Due to the inherent statistical nature of the presented offset recovery, we quantify the average-case TC. Therefor we employ the average number of iterations over the inner loop in Algorithm 2, i.e.

$$\bar{N}_{\text{loop}} = p_{\text{det}} N_{\text{s,g}} N_\ell, \quad \text{with} \quad (20)$$

$$p_{\text{det}} = 1 - (1 - p_{\text{sig}})(1 - p_{\text{noise}}). \quad (21)$$

Evaluating \bar{N}_{loop} along the lines of Fig. 4 results in the TCs depicted in Fig. 5.

Sublinear TC is achieved for $p_{\text{noise}} = 0$, as well as for $p_{\text{noise}} = 0.22 p_{\text{sig}}$, which corresponds to a QBER of 11%, the upper limit for QKD. For $p_{\text{noise}} = 0$ the TC can be fitted by the poly-logarithmic function

$$f(n) = a(\log_2 n)^b. \quad (22)$$

With $a \approx 2.9, b \approx 1.3$ ($a \approx 4.9, b \approx 3.2$) for no (max.) interleaving the relative deviation is bounded by 2.9% (5.1%) over the range shown in Fig. 5, which entails all offsets relevant to practical QKD implementations.

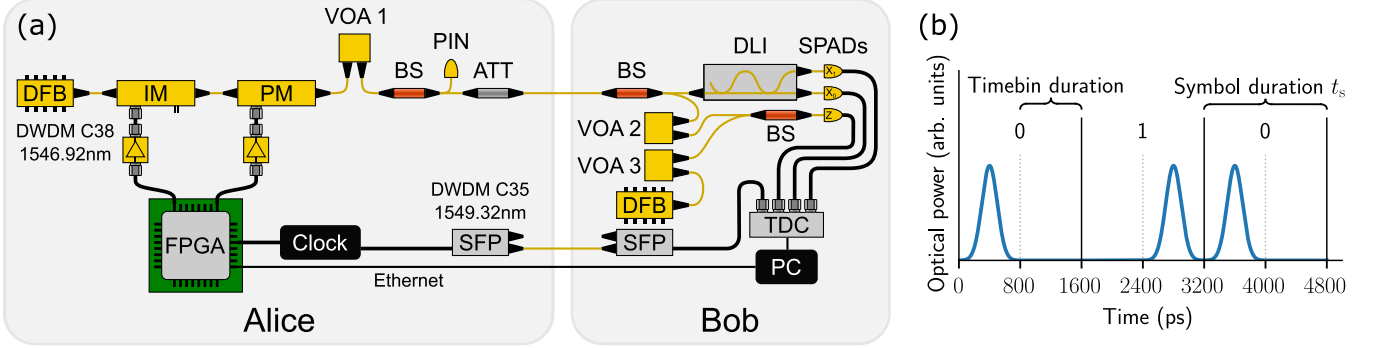


FIG. 6. Experimental setup. In (a) the systems for Alice and Bob are shown, as they were used for verifying the analytically derived success probabilities (Section III). The clock beat was transmitted via fiber. Using VOA 2, the channel attenuation was applied in the Z-basis only, such that the X-basis QBER could be used to independently check for synchronization success. Additional optical noise was added directly in front of the Z-basis detector via a second laser and could be tuned via VOA 3. The symbol encoding, using binary PPM, is shown in (b) for the example symbol sequence "010". For the experiments a symbol duration $t_s = 1600$ ps was used. FPGA: field-programmable gate array; SFP: Small form-factor pluggable; DFB: Distributed-feedback laser; IM: Intensity modulator; PM: Phase modulator; VOA: Variable optical attenuator; BS: Beam splitter; PIN: Photodiode; ATT: Fix attenuator; DLI: Delay-line interferometer; SPAD: Single-photon avalanche detector; TDC: Time digital converter.

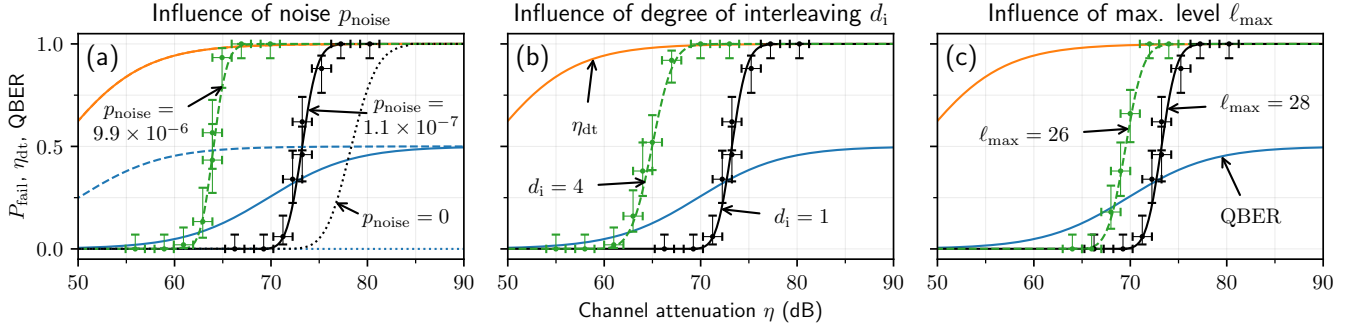


FIG. 7. Comparison of experimental failure probabilities P_{fail} and their modelling for different configurations. In (a) the solid black curve depicts P_{fail} for maximum level $\ell_{\text{max}} = 28$, degree of interleaving $d_i = 1$, and no added optical noise. The dashed green line shows P_{fail} for optical noise added on the detector. The dotted black curve shows the theoretical results for the case of no noise counts. The solid (dashed) blue curve depicts the expected QBER for the configuration without (with) added noise. The red curve shows the relative dead-time-induced reduction η_{dt} of the effective detector efficiency. The error bars represent the 95%-CI for an uninformed prior. In (b) and (c) the dashed green line shows P_{fail} for an increased d_i , and a reduced ℓ_{max} , respectively.

Only for constant values of $p_{\text{noise}} > 0$ the TC takes super-linear complexity in the regime past the point with a QBER of 11 %, given by the intersection with the curve for $p_{\text{noise}} = 0.22 p_{\text{sig}}$. However, this regime is of little importance for QKD, since it does not allow for the generation of secure keys.

Hence, the clock offset recovery Alogirthm 2 has polylogarithmic average-case TC for the parameter regime relevant for QKD.

V. EXPERIMENT

We experimentally validated our method and compared it with the analytically derived success probabilities, cf. Section III. Therefor, iQSync was implemented

in our timebin-phase QKD system, employing the finite-size 1-decoy timebin-phase BB84 protocol [38, 39], using two timebins per qubit and a qubit transmission rate of 625 MHz.

The system was used in the experimental configuration as shown in Fig. 6. At Alice, the pattern was generated in real-time on an FPGA (Xilinx Ultrascale+ VU13P), using a synthesized AES-CTR module for the random level choice, if $d_i > 1$, cf. Algorithm 1. The transmitted mean photon number per symbol was set to 1 during the synchronization.

The channel attenuation was realized using a variable optical attenuator (VOA) in front of the Z-basis detector, which was used for the synchronization. This setup allowed to use the X-basis QBER to reliably identify successful synchronizations, even at very high channel atten-

uations for which QBERs near 50% were observed in the Z-basis. Stirling-cooled SPADs (ID Quantique ID230) with a dead-time $\tau_{dt} = 96.3\ \mu\text{s}$ and single photon detection efficiency $\eta_{det} = 0.154$ were used. Offset recovery (Algorithm 2) was implemented in a few lines of C++ code and evaluated during real-time operation.

Comparative outcomes between experimental failure probabilities, P_{fail} , and their modeling are depicted in Fig. 7. The baseline condition is represented by the solid black curves, established through a maximum level of $\ell_{max} = 28$, a degree of interleaving of $d_i = 1$, and the absence of additional optical noise, leading to $p_{noise} = 1.1 \times 10^{-7}$, caused by detector dark counts. The resulting pattern has a duration of 24.9 s and allows to recover offsets of up to $\Delta_{max} = 215\ \text{ms}$.

Fig. 7(a) demonstrates the introduction of optical noise to the detector, leading to a noise detection probability of $p_{noise} = 9.9 \times 10^{-6}$. Fig. 7(b) denotes a condition wherein the degree of interleaving was increased to $d_i = 4$ and Fig. 7(c) depicts a situation where the maximum level was decreased to $\ell_{max} = 26$. For each observation point, the system was started 50 times, and successful synchronizations were counted. The channel attenuation, as shown on the horizontal axis, includes all losses between Alice and the Z-basis detector, and encompasses the detector efficiency as well as its efficiency reduction induced by dead-time.

For $\ell_{max} = 28$ and $d_i = 4$ the synchronization pattern spanned 6.9 s, leading to 4372 ± 63 detections with reliable recovery (49 out of 50 runs) of offsets up to 215 ms at 61.0 dB channel attenuation, cf. Fig. 7(b).

For $\ell_{max} = 28$ and $d_i = 1$ the synchronization pattern spanned 24.9 s, leading to 3056 ± 62 detections with reliable recovery (47 out of 50 runs) of offsets up to 215 ms at 71.2 dB channel attenuation, cf. Fig. 7(b).

Furthermore, iQSync has successfully been used by our QKD system in combination with fiber and free-space links (publications in preparation).

In summary, these experimental outcomes demonstrate the method's performance and robust conformity with the theoretical modeling. As a result, the theoretical model outlined in Section III can be effectively utilized to discern optimal values for ℓ_{max} and d_i for a given link configuration, and our synchronization method can be used for channel attenuations exceeding 70 dB.

VI. CONCLUSION

We introduced iQSync, a synchronization method suited for low-level hardware implementations. iQSync works by successively identifying the binary representation bits of the clock offset, starting from the least significant bit, and interleaving the requisite patterns to reduce the total pattern duration. The pattern is determined by two parameters: its maximum level ℓ_{max} , defining the maximum recoverable offset, and the degree of interleaving d_i , by which the total pattern duration

can be reduced. For the random level interleaving we used AES-CTR random number expansion, but simpler algorithms should suffice.

We derived an analytical expression for the success probability, and the average-case time complexity of the recovery algorithm was found to be poly-logarithmic for all settings relevant to QKD using the BB84 protocol, i.e. QBERs below 11%. Furthermore, we demonstrated excellent agreement between the analytical results and experimental measurements for different link and parameter configurations. Reliable synchronization, requiring only a few thousand iterations over a simple loop, was demonstrated for total channel attenuations exceeding 70 dB.

Greater channel losses could readily be compensated by using more than one photon per symbol during the synchronization, enabling operation even under most adverse conditions [3]. In prepare-and-measure QKD systems the number of photons per qubit can often readily be adjusted using Alice's VOA. Alternatively, the tolerable channel attenuation for a given ℓ_{max} can also be increased by prolongation of the level patterns, which requires a slight modification of Algorithms 1 and 2. Hence, our method is well suited for prepare-and-measure QKD systems, even for noisy channels with high attenuation.

Furthermore, iQSync could also be of interest for other applications, such as LIDAR, optical deep space communication, or communication out of line of sight.

The presented experimental results and successful operation during the last three years demonstrate the reliability and applicability of iQSync to real communication networks.

VII. ACKNOWLEDGEMENTS

We thank Andy Schreier for valuable feedback on this manuscript.

Large Language Models were used during writing to polish and lightly edit some passages.

This research was conducted within the scope of the project QuNET, funded by the German Federal Ministry of Education and Research (BMBF) in the context of the federal government's research framework in IT-security "Digital. Secure. Sovereign."

VIII. AUTHOR CONTRIBUTIONS

N.W. proposed and directed the research. J.K. developed the synchronization method with guidance from N.W. J.K. conceived and implemented the algorithms, including the example Python implementation in the Supplemental Material [37]. J.H. implemented the transmission algorithm on the FPGA. J.K. performed the experiments, evaluated the measurement data, analytically derived the success probability, and conducted the time complexity analysis. R.F. acquired the funding. J.K.

wrote the manuscript. All authors discussed the results

and reviewed the manuscript.

[1] C. H. Bennett and G. Brassard, Quantum cryptography: Public key distribution and coin tossing, *Proceedings of the IEEE International Conference on Computers, Systems and Signal Processing* , 175 (1984).

[2] C. Portmann and R. Renner, Security in quantum cryptography, *Reviews of Modern Physics* **94**, 025008 (2022).

[3] A. Boaron, G. Boso, D. Rusca, C. Vulliez, C. Autebert, M. Caloz, M. Perrenoud, G. Gras, F. Bussières, M.-J. Li, D. Nolan, A. Martin, and H. Zbinden, Secure Quantum Key Distribution over 421 km of Optical Fiber, *Physical Review Letters* **121**, 190502 (2018).

[4] D. Gottesman, Hoi-Kwong Lo, N. Lütkenhaus, and J. Preskill, Security of quantum key distribution with imperfect devices, in *International Symposium on Information Theory, 2004. ISIT 2004. Proceedings.* (IEEE, Chicago, Illinois, USA, 2004) pp. 135–135.

[5] G. P. Agrawal, *Fiber-Optic Communication Systems*, 4th ed., Wiley Series in Microwave and Optical Engineering (Wiley, Hoboken, NJ, 2010).

[6] J. C. Bienfang, A. J. Gross, A. Mink, B. J. Hershman, A. Nakassis, X. Tang, R. Lu, D. H. Su, C. W. Clark, C. J. Williams, E. W. Hagley, and J. Wen, Quantum key distribution with 1.25 Gbps clock synchronization, *Optics Express* **12**, 2011 (2004).

[7] A. Tanaka, M. Fujiwara, S. W. Nam, Y. Nambu, S. Takahashi, W. Maeda, K.-i. Yoshino, S. Miki, B. Baek, Z. Wang, A. Tajima, M. Sasaki, and A. Tomita, Ultra fast quantum key distribution over a 97 km installed telecom fiber with wavelength division multiplexing clock synchronization, *Optics Express* **16**, 11354 (2008).

[8] Y. Liu, T.-Y. Chen, J. Wang, W.-Q. Cai, X. Wan, L.-K. Chen, J.-H. Wang, S.-B. Liu, H. Liang, L. Yang, C.-Z. Peng, K. Chen, Z.-B. Chen, and J.-W. Pan, Decoy-state quantum key distribution with polarized photons over 200 km, *Optics Express* **18**, 8587 (2010).

[9] N. Walenta, A. Burg, D. Caselunghe, J. Constantin, N. Gisin, O. Guinnard, R. Houlmann, P. Junod, B. Korzh, N. Kulesza, M. Legré, C. W. Lim, T. Lunghi, L. Monat, C. Portmann, M. Soucarros, R. T. Thew, P. Trinkler, G. Trolliet, F. Vannel, and H. Zbinden, A fast and versatile quantum key distribution system with hardware key distillation and wavelength multiplexing, *New Journal of Physics* **16**, 013047 (2014).

[10] B. Korzh, C. C. W. Lim, R. Houlmann, N. Gisin, M. J. Li, D. Nolan, B. Sanguinetti, R. Thew, and H. Zbinden, Provably Secure and Practical Quantum Key Distribution over 307 km of Optical Fibre, *Nature Photonics* **9**, 163 (2015).

[11] J. F. Dynes, W. W.-S. Tam, A. Plews, B. Fröhlich, A. W. Sharpe, M. Lucamarini, Z. Yuan, C. Radig, A. Straw, T. Edwards, and A. J. Shields, Ultra-high bandwidth quantum secured data transmission, *Scientific Reports* **6**, 35149 (2016).

[12] N. T. Islam, C. C. W. Lim, C. Cahall, J. Kim, and D. J. Gauthier, Provably secure and high-rate quantum key distribution with time-bin qudits, *Science Advances* **3**, e1701491 (2017).

[13] P. Zhang, D. K. L. Oi, D. Lowndes, and J. G. Rarity, Timing and synchronisation for high-loss free-space quantum communication with Hybrid de Bruijn Codes, *IET Quantum Communication* **2**, 80 (2021).

[14] F. Berra, C. Agnesi, A. Stanco, M. Avesani, M. Kuklewski, D. Matter, P. Villoresi, and G. Vallone, Synchronization of quantum communications over an optical classical communications channel, *Applied Optics* **62**, 7994 (2023).

[15] T. Jennewein, C. Simon, G. Weihs, H. Weinfurter, and A. Zeilinger, Quantum Cryptography with Entangled Photons, *Physical Review Letters* **84**, 4729 (2000).

[16] I. Marcikic, A. Lamas-Linares, and C. Kurtsiefer, Free-space quantum key distribution with entangled photons, *Applied Physics Letters* **89**, 101122 (2006).

[17] R. Ursin, F. Tiefenbacher, T. Schmitt-Manderbach, H. Weier, T. Scheidl, M. Lindenthal, B. Blauensteiner, T. Jennewein, J. Perdigues, P. Trojek, B. Ömer, M. Fürst, M. Meyenburg, J. Rarity, Z. Sodnik, C. Barbieri, H. Weinfurter, and A. Zeilinger, Entanglement-based quantum communication over 144 km, *Nature Physics* **3**, 481 (2007).

[18] C. Erven, C. Couteau, R. Laflamme, and G. Weihs, Entangled quantum key distribution over two free-space optical links, *Optics Express* **16**, 16840 (2008).

[19] C. Ho, A. Lamas-Linares, and C. Kurtsiefer, Clock synchronization by remote detection of correlated photon pairs, *New Journal of Physics* **11**, 045011 (2009).

[20] E. Fitzke, L. Bialowons, T. Dolejsky, M. Tippmann, O. Nikiforov, T. Walther, F. Wissel, and M. Gunkel, Scalable Network for Simultaneous Pairwise Quantum Key Distribution via Entanglement-Based Time-Bin Coding, *PRX Quantum* **3**, 020341 (2022).

[21] C. Spiess, S. Töpfer, S. Sharma, A. Kržič, M. Cabréjo-Ponce, U. Chandrashekara, N. L. Döll, D. Rieländer, and F. Steinlechner, Clock Synchronization with Correlated Photons, *Physical Review Applied* **19**, 054082 (2023).

[22] H. Takenaka, A. Carrasco-Casado, M. Fujiwara, M. Kitamura, M. Sasaki, and M. Toyoshima, Satellite-to-ground quantum-limited communication using a 50-kg-class microsatellite, *Nature Photonics* **11**, 502 (2017).

[23] L. Calderaro, A. Stanco, C. Agnesi, M. Avesani, D. Dequal, P. Villoresi, and G. Vallone, Fast and Simple Qubit-Based Synchronization for Quantum Key Distribution, *Physical Review Applied* **13**, 054041 (2020).

[24] R. D. Cochran and D. J. Gauthier, Qubit-Based Clock Synchronization for QKD Systems Using a Bayesian Approach, *Entropy* **23**, 988 (2021).

[25] C.-Z. Wang, Y. Li, W.-Q. Cai, W.-Y. Liu, S.-K. Liao, and C.-Z. Peng, Synchronization using quantum photons for satellite-to-ground quantum key distribution, *Optics Express* **29**, 29595 (2021).

[26] C. Agnesi, D. Scalcon, M. Avesani, L. Calderaro, G. Folletto, A. Stanco, G. Vallone, and P. Villoresi, Time-bin Quantum Key Distribution exploiting the iPOGNAC polarization modulator and Qubit4Sync temporal synchronization, in *Optical Fiber Communication Conference (OFC) 2022* (Optica Publishing Group, San Diego, California, 2022) p. M3I.5.

[27] C. Spiess and F. Steinlechner, Clock synchronization with pulsed single photon sources, *Quantum Science and Technology* **9**, 015019 (2023).

[28] M. Zahidy, D. Ribezzo, R. Müller, J. Riebesehl, A. Zavatta, M. Galili, L. K. Oxenløwe, and D. Bacco, Single-photon-based clock analysis and recovery in quantum key distribution, *AVS Quantum Science* **5**, 041403 (2023).

[29] A. Lohrmann, A. Zhai, and M. Mohageg, Classical clock synchronization for quantum communications using the quantum channel, *Applied Optics* **62**, 8567 (2023).

[30] T. Scheidl, R. Ursin, A. Fedrizzi, S. Ramelow, X.-S. Ma, T. Herbst, R. Prevedel, L. Ratschbacher, J. Kofler, T. Jennewein, and A. Zeilinger, Feasibility of 300 km quantum key distribution with entangled states, *New Journal of Physics* **11**, 085002 (2009).

[31] S. Ecker, B. Liu, J. Handsteiner, M. Fink, D. Rauch, F. Steinlechner, T. Scheidl, A. Zeilinger, and R. Ursin, Strategies for achieving high key rates in satellite-based QKD, *npj Quantum Information* **7**, 5 (2021).

[32] R. Lafler and R. N. Lanning, Quantum Time Transfer: A Practical Method for Lossy and Noisy Channels, *Physical Review Applied* **20**, 024064 (2023).

[33] D. Wang, L. Zhou, and Y. Zhao, Robust frame synchronization for continuous-variable quantum key distribution with coherent states, *Optics Express* **31**, 43163 (2023).

[34] N. Walenta, Quantum communication synchronization and alignment procedure, European Patent EP3787220, European Patent Office (2023).

[35] J. W. Cooley and J. W. Tukey, An Algorithm for the Machine Calculation of Complex Fourier Series, *Mathematics of Computation* **19**, 297 (1965).

[36] M. Braithwaite, Quantum channel synchronization, European Patent EP3754895, European Patent Office (2020).

[37] See Supplemental Material at [URL will be inserted by publisher] for an example Python implementation and full link simulation.

[38] D. Rusca, A. Boaron, F. Grünenfelder, A. Martin, and H. Zbinden, Finite-key analysis on the 1-decoy state QKD protocol, *Applied Physics Letters* **112**, 171104 (2018).

[39] F. Moll, J. Krause, N. Walenta, R. Freund, E. Peev, A. Reeves, R. Rüddenklaau, A. Ferenczi, L. Macri, S. Häusler, J. P. Labrador, M.-T. Hahn, J. Poliak, D. Orsucci, and F. Fohlmeister, Link technology for all-optical satellite-based quantum key distribution system in C-/L-band, in *2022 IEEE International Conference on Space Optical Systems and Applications (ICSOS)* (IEEE, Kyoto City, Japan, 2022) pp. 275–280.

[40] The validity of this approximation should be checked for each context. Requiring the 3σ interval of the distribution to be completely contained within the interval $[0, 1]$ yields the requirement $9(1 - p)/(np) < 1$, which is satisfied for all measurements shown in Fig. 7.